Rods-on-string idealization captures semiflexible filament dynamics

Preethi L. Chandran and Mohammad R. K. Mofrad*
Molecular Cell Biomechanics Laboratory, Department of Bioengineering, University of California, Berkeley, California 94720, USA
(Received 24 April 2008; published 13 January 2009)

We present an approach to modeling the two-dimensional Brownian dynamics of semiflexible filaments in the worm-model description as uniform, isotropic, and continuously flexible. Experimental observations increasingly show that the mechanical behavior of semiflexible filament networks departs from conventional knowledge. A force-balance-based dynamic simulation of the filament networks has multiple advantages as an approach to understanding their anomalous mechanics. However, a major disadvantage is the difficulty of capturing filament hydrodynamics and bending mechanics in a computationally efficient and physically consistent manner. To that end, we propose a strategy for modeling semiflexible filaments which involves idealizing a semiflexible filament as a contiguous string of flexible rods, and considering the Brownian forces on it as Einsteinian-like point normal and tangential forces. By idealizing the filament as a string of rods, we avoid the complex hydrodynamic treatment involved in beads-on-string idealizations, and implement large-deflection beam mechanics and filament inextensibility in a natural manner, while reducing the computational size of the problem. By considering the Brownian forces as point normal and tangential forces, we decompose the Brownian forces on straight and curved segments into a combination of classical resultant forces and couples whose distribution is shown to be governed by the rod diffusion coefficients. The decomposition allows solution of the Euler beam equations to second-order continuity between segments and fifth-order continuity within segments. We show that the approach is physically consistent by capturing multiple Brownian phenomena ranging from the rigid to the semiflexible limit: the translational and rotational diffusion of rigid rods; the thermal fluctuation of semirigid cantilever filaments; and the shape, bending, and time relaxation of freely diffusing, semiflexible actin filaments.

DOI: 10.1103/PhysRevE.79.011906 PACS number(s): 87.16.Ka, 87.16.Ln, 87.15.A−

I. INTRODUCTION

The cytoskeleton is made up of a network of filamentous proteins which by their assembly dynamics and mechanics mediate cell shape, migration, and force transfer [1,2]. The three broadly important cytoskeletal filaments are actin, microtubules, and intermediate filaments, with diameters of 8, 25, and 10 nm, respectively [2]. These filaments are classified as semiflexible, because the length over which their contour angles correlate, i.e., the persistence length, is on the order of the lengths typically found in the cytoskeleton. Consequently, unlike in typical flexible polymers, the entropic contribution to the free energy is very small for these filaments, and the enthalpic or strain energy contribution plays a larger role. A popular conception of the free-energy state of a semiflexible filament is the worm model of Kratky and Porod [3]. It likens a semiflexible filament to a continuously flexible and isotropic rod, with the bending at any point governed by Euler beam mechanics. Consequently, for a given conformation Ω of a semiflexible filament, the total free energy $H(\Omega)$ is obtained by integrating over the bending energy of infinitesimal beams at every point of its contour length L,

$$H(\Omega) = \frac{EI}{2}\int_0^L dl\left(\frac{\partial\theta(l)}{\partial l}\right)^2, \tag{1}$$

where $\theta(l)$ is the filament angle at contour length l. The proportionality constant EI is the filament's bending stiffness or flexural rigidity, with E being the Young's modulus in extension and I being the cross-sectional inertia [2,4]. Since the above free energy of the filament is quadratic in θ [Eq. (1)], the probability of finding a particular filament conformation, $p(\Omega)$, at thermal equilibrium, is given by the Boltzmann distribution [2,5],

$$p(\Omega) = \frac{1}{Z}\exp\left(-\frac{H(\Omega)}{KT}\right) = \frac{1}{Z}\exp\left[-\frac{EI}{2KT}\int_0^L dl\left(\frac{\partial\theta(l)}{\partial l}\right)^2\right], \tag{2}$$

where K is the Boltzmann constant, T is the temperature, and Z is a normalization constant. Equation (2) defines a unique material constant, the persistence length (L_p),

$$L_p = \frac{EI}{KT}, \tag{3}$$

which captures the competition between flexural rigidity and thermal energy in determining the conformation or shape of the filament. Using Eq. (2) and the equipartition theorem [mean energy of $KT/2$ for one degree of bending freedom in two dimensions (2D)], the filament's persistence length can be determined from the decorrelation of the filament's tangent angles along its contour l [2],

$$\langle\cos\theta(l)\cos\theta(0)\rangle = \exp\left(-\frac{l}{2L_p}\right). \tag{4}$$

Due to its nonlinear nature, Eq. (2) can be used to determine only a few properties of semiflexible filaments analytically, notably the mean squared end-to-end distance and the persis-

*Corresponding author. mofrad@berkeley.edu

tence length. Its use to solve for semiflexible filament behavior is further complicated by the need to impose filament inextensibility as an external constraint [6,7].

The ability to solve for semiflexible filament behavior is critical to understanding the behavior of their networks, which have increasingly been found to show mechanical properties that differ from those of flexible polymer networks. Networks of actin filaments show a reversible stress-softening in compression [8], whereas any known stress softening in flexible polymer networks has been due to failure and yielding, and is not reversible. Also, networks of semiflexible polymers show negative normal stresses in shear which tend to pull the shear plates inward [9]. Networks of flexible polymers, on the other hand, show positive normal stresses in shear or push the shear plates outward. Also, networks of semiflexible filaments show nonlinear shear stiffening much larger than that observed with networks of flexible polymers [10]. It is unclear whether the anomalies can be explained within the worm model description of a network filament as a uniform flexible rod; or if additional complexities due to nonhomogeneous protein microstructure need to be accounted for [11]. It is also unclear what the underlying filament deformations are that lead to such a network behavior [12,13].

Dynamic or force-balance-based simulation presents a way to avoid the mathematical complexities with analytically solving for semiflexible filament behavior, and for understanding the microstructural basis of the above network behavior. At the filament level, the chief advantages of dynamic simulation are that (1) the small-fluctuation approximations required for analytically solving semiflexible filament equations [Eq. (2)] are no longer necessary; (2) a force-balance-based description of Brownian motion, Langevin dynamics, is well developed [14,15]; and (3) a form of filament inextensibility can be naturally imposed. From the network point of view, the chief advantages of dynamic simulation are that (1) the pointwise displacement and force constraints characterizing filament cross linking in a network are easily imposed, unlike in free-energy models; and (2) by requiring the forces to balance, no extraneous assumption on filament or cross-link kinematics needs to be made, unlike in the statistical models. Even though the computational cost of dynamic simulation is higher, because all relevant centers of force balance must be accounted for, one cannot overstate the importance of these simulations in instructing the kinematic assumptions of free-energy and statistical models.

A serious disadvantage with the dynamic or force-balance approach, however, is our limited knowledge of the nature and geometry of the forces and their points of action. This is particularly true in the case of semiflexible filaments, where the force balance is complicated by the continuous and nonlinear nature of filament bending and by the constraint of filament inextensibility. A number of these issues can be resolved by increasing the computational cost of modeling a single semiflexible filament. However, increasing the computational cost of modeling a single filament seriously limits the ability to scale up to multiple-filament networks. In this paper, we focus only on the central problem of dynamically simulating semiflexible filaments in a physically consistent but computationally efficient manner. We propose a different way of idealizing a semiflexible filament that overcomes many of the above problems. To that end, we first illustrate the difficulties with dynamically simulating semiflexible filaments, in the context of the popular string-of-beads idealization.

In a weak force field (F^P), a particle is assumed to drift with a velocity (v) that is proportional to the force, and the proportionality constant is known as the frictional coefficient (ξ). In Langevin dynamics, this linear relation between particle velocity and external force is extended to describe the particle's response to random Brownian forces (F^B) generated by incessant collision with solvent molecules [15],

$$\xi v(t) = F^P(t) - F^B(t), \tag{5}$$

where F^P is the conserved force, a function of the particle position and/or conformation. By requiring the solution of Eq. (5) to match the Boltzmann distribution, two key relations are obtained:

$$D = \frac{KT}{\xi}, \tag{6}$$

$$\langle F^B(t)F^B(t')\rangle = 4KT\xi\delta(t-t'). \tag{7}$$

Note that all expressions in this study pertain to two-dimensional space. Equation (6) allows for a microscale particle feature like the frictional coefficient to be determined from macroscale observations of particle diffusion, and gave one of the first numerical estimates for the Boltzmann constant [16]. Equation (7) suggests that the Brownian fluctuation motion is intimately linked to the viscous forces on the particle, and allows for the determination of viscoelastic relaxation times from the Brownian fluctuation motions [16–18].

For fluctuating semiflexible filaments, the conserved force F_p is replaced by the internal bending force of the worm model, and Eq. (5) appears as

$$\xi v(t) = EI\frac{d^2\theta}{dl^2} - F(t). \tag{8}$$

For ease of representation we have denoted the Brownian force in the above expression by F instead of F^B, and will maintain the representation throughout the rest of the paper.[1] In simulating a semiflexible filament, one first needs to determine the points on the filament at which the fluctuation, dissipation, and elastic forces in Eq. (8) can be applied and balanced. A common approach is to discretize the filament into a string of beads, and apply viscous and Brownian forces well known for a sphere at each bead center. However, the discretization into beads leads to an error in the hydrodynamics that vanishes only as the bead number tends to infinity [15]. For instance, the diffusion coefficient of a rigid representation of a string of beads matches that of a rigid cylindrical rod only at infinite bead number [15]. Corrections

[1]Note that in Eq. (8), F indicates force and not force density. Also, the filaments are assumed inextensible and therefore no tension term appears in it. See the discussion of Eqs. (9) and (10) for how filament incompressibility is ensured.

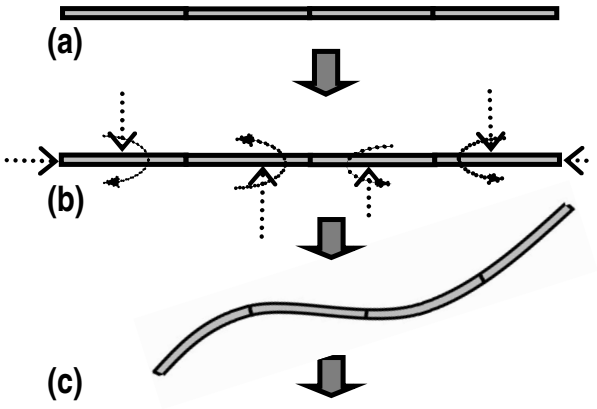

FIG. 1. Modeling of filament fluctuation dynamics. (a) Discretize filament into string of rod segments. (b) Determine resultant Brownian forces and couple on each segment. (c) Solve for the large-deflection beam mechanics and filament displacement to balance Brownian forces. Repeat from step (b) for new filament configuration.

such as scaling up of bead size and use of overlapping beads have been proposed to match rod diffusion data, but the corrections have not been found uniformly applicable [19–21]. In addition, the discretization of a continuous filament leads to errors in determining bending angles and contour length. In order to avoid the large increase in computation that comes with increasing bead number, the error is usually accepted, with the argument that over long-time simulations of a large number of filaments the errors average out [15]. To our knowledge, there are very few publications where semiflexible filament dynamics have been captured in a physically consistent manner for a range of L_p/L, i.e., from rigid to semiflexible, and validated rigorously [22].

In this paper we propose an idealization of a semiflexible filament as a string of continuously flexible rods. It bypasses the above discretization errors with decreased computational cost in the following ways: (1) by discretizing into rods, Euler beam mechanics and filament inextensibility can be naturally imposed; (2) the errors in hydrodynamics that come with discretization into beads are preempted; and (3) since a single rod replaces a number of beads, a significant decrease in computational time and effort is obtained. The string-of-rods approach is made possible by two implementations. First, we show that for a curved rod much smaller than the persistence length the Brownian forces and hydrodynamics can be derived as an extension of those of a straight rod. Second, we show that the large-deflection Euler beam mechanics can be solved at each rod segment to second-order continuity in angle between segments and to fifth-order continuity within the segment, thereby naturally preserving the inextensibility constraint. A schematic of the solution strategy is shown in Fig. 1. We show that, with this approach, the dynamics of a semiflexible filament can be captured from its rigid to semirigid to semiflexible limit.

In the version of the model presented in this paper, we look only at the dynamic behavior of semiflexible filaments that results from their shape as a uniform, slender, and continuously flexible rod. We neglect any complexities due to the nonhomogeneous internal microstructure. Such a shape-based approximation of dynamics has been shown valid for densely packed systems like proteins in which the large-amplitude low-frequency deformations, usually involved in macromolecular function, are found to be universally determined by macromolecular shape [23,24].

II. MATERIALS AND METHODS

Our formulation likens a semiflexible filament to a continuous string of rod segments. We make two basic assumptions on the nature of the Brownian forces exerted on the filament segment. (1) The Brownian force on a segment that is a part of a filament is the same as when the segment is free in solution, provided hydrodynamic screening and end effects are neglected. (2) The Brownian force on a segment is not affected by the bending capacity of the segment. Therefore, at any instant, the Brownian force on a segment that is a part of a flexible filament is assumed equal to the Brownian force that would occur on the same segment were it freely diffusing, rigid, and locked in its shape at the instant of force application. Based on this idealization, we make the following three assertions as to how the Brownian force on a segment of a semiflexible filament is determined, and how the resulting segment deformation is determined from large-deflection Euler beam mechanics. We prove these assertions in Secs. II A–II C.

(1) For a rigid, straight segment, the net effect of the Brownian forces on its surface can be captured by a combination of a single resultant force and a couple acting at the segment center. The variance of these resultants is determined by the translational and rotational diffusion coefficients of the segment.

(2) For a rigid, curved segment, the net effect of the Brownian forces *projected* in any direction can be captured as single resultant force and a couple at the center of the segment projection in that direction. The variance of these resultants is determined by the translational and rotational diffusion coefficients for the projected length.

(3) For flexible segments much smaller than the persistent length the net moment balance is completely determined by the resultants of the Brownian forces projected in two mutually perpendicular directions. For such a projection of the Brownian forces, the large-deflection Euler beam equations can be solved to fifth-order continuity in angle within each segment, and to second-order continuity in angle between segments.

Solution of the large-deflection Euler beam equations involves not making the small-strain assumptions on filament curvature. In x and y coordinates, the filament curvature is given as

$$\frac{\partial \theta}{\partial l} = \frac{\partial^2 y/\partial x^2}{[1+(\partial y/\partial x)^2]^{3/2}}, \tag{9}$$

where θ is the angle along the contour length l. The above expression is nonlinear, and makes the beam equations difficult to solve. On the other hand, a small-deflection assumption (small $\partial y/\partial x$) allows the denominator to go to 1, giving the curvature as

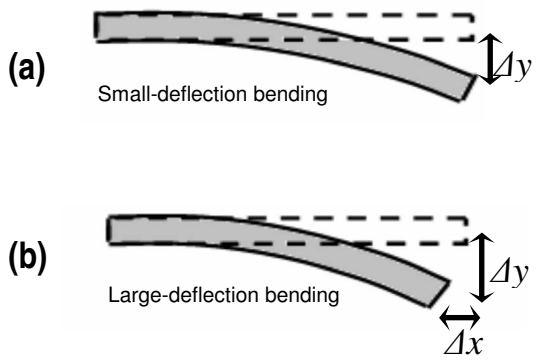

FIG. 2. Small-deflection (a) versus large-deflection (b) bending dynamics of a cantilever. Small-deflection theory does not account for the inward deflection in the $-x$ direction that accompanies any deflection in the $-y$ direction, consequently overpredicting the length of the deformed cantilever.

$$\frac{\partial \theta}{\partial l} \approx \frac{\partial^2 y}{\partial x^2}. \tag{10}$$

The small-deflection or small-strain approximation is commonly made in structural mechanics where the deflections are indeed small. The approximation gives about 4% error at 10% deflection [25], with the error increasing nonlinearly thereafter. However, the small-deflection assumption used along with a Lagrangian frame of reference introduces a spurious lengthening in the bending filament, i.e., a filament deflection in the vertical direction is not accompanied by a horizontal inward deflection to preserve filament length (Fig. 2). Therefore, models of semiflexible filaments which use the small-deflection assumption typically add on an external constraint forcing the filament to be inextensible.

A. Brownian force on a rigid segment

The diffusion of rigid cylindrical rods is described by three independent diffusion coefficients D_n, D_p, and D_r, which govern the rod's translation normal (D_n) and parallel (D_p) to itself, and the rod's rotation (D_r). The mathematical expressions for these coefficients have been well studied, standardized, and shown to match experimental data [26]. For slender rods, the three diffusion coefficients are

$$D_p = \frac{KT}{8\pi\eta L} \ln\left(\frac{L}{d}\right), \tag{11}$$

$$D_n = \frac{KT}{4\pi\eta L} \ln\left(\frac{L}{d}\right), \tag{12}$$

$$D_r = \frac{3KT}{8\pi\eta L^3} \ln\left(\frac{L}{d}\right), \tag{13}$$

where d is the filament diameter and η is the solvent viscosity. Without the logarithmic (ln) term, the above expression can be derived by idealizing a rod to a string of *infinitesimal* beads, and considering the Brownian forces on them (Kirkwood theory) [15]. The ln term captures a super-posed hydrodynamic effect from the interaction between the beads [15], as though the extension of the segment screens and reduces the local drag on it. Experimentally, the diffusion coefficients are determined from the mean square of the net displacement or rotation occurring in intervals of Δt,

$$D_i = \frac{\langle \Delta z_i \Delta z_i \rangle}{2\Delta t}, \tag{14}$$

where $i=n,p,r$. The parallel and normal directions for the interval Δt are usually assigned based on the rod's orientation at the beginning of the interval. The denominator in Eq. (14) includes a factor of 2 instead of the factor of 4 that is usually encountered with 2D diffusion, particularly of spherical particles. This is because, for a cylindrical rod diffusing in 2D, there is only one degree of freedom for it to diffuse parallel or normal to itself, and for it to rotate in plane.

A fundamental tenet in rigid-body mechanics is that the net effect of any set of surface forces can be captured by (1) a single resultant force acting at the center of mass and equal to the vector sum of all forces on the rod, and (2) a single resultant couple acting at the center of mass and equal to the sum of all moments about the center of mass. Brownian motion of a rod can be idealized as occurring from the net effect of all the point tangential and point normal forces acting on its surface from collision with the solvent molecules. In such a case, any rotation of the rod must be due to the net moment that the point normal Brownian forces exert about its center. Also, the rod's diffusion coefficients, by virtue of being measured from net displacements and rotations of the rod [Eq. (14)], are likely to govern the variance of the resultant forces and couple. That is, in the expression obtained by combining Eqs. (6) and (7),

$$\langle F_i \,.\, F_i \rangle = \frac{4(KT)^2}{D_i'}. \tag{15}$$

F_i is expected to be the resultant of the point normal and parallel Brownian forces for $i=n,p$ and the resultant of the moments due to the normal Brownian forces on the rod for $i=r$. The idealization is depicted in Fig. 3.

In order to prove the above ideas, we use a version of the diffusion coefficients in Eqs. (11)–(13) which does not include the correction term for hydrodynamic screening (ln term), and denote it by D_i', with $i=n,p,r$. We do not include the correction because hydrodynamic screening is a second-order effect and not primarily determined by the Brownian forces. We do include the ln term in our simulations, but as a constant prefactor multiplying D_i', determined by the overall filament dimensions and acting as if to condition the local Brownian response equally everywhere on the rod.

For a Gaussian distribution, the variance of a sum of n samples is equal to the sum of the variance of each sample, i.e.,

$$\begin{aligned} \mathrm{Var}(X_1 + \cdots + X_n) &= \mathrm{Var}(X_1) + \cdots + \mathrm{Var}(X_n) \\ &= n\,\mathrm{Var}(X), \quad X_i \in X. \end{aligned} \tag{16}$$

For Brownian motion, the total number of point forces due to collision must be proportional to the length of the rod, for rods of the same diameter. If the normal and parallel diffu-

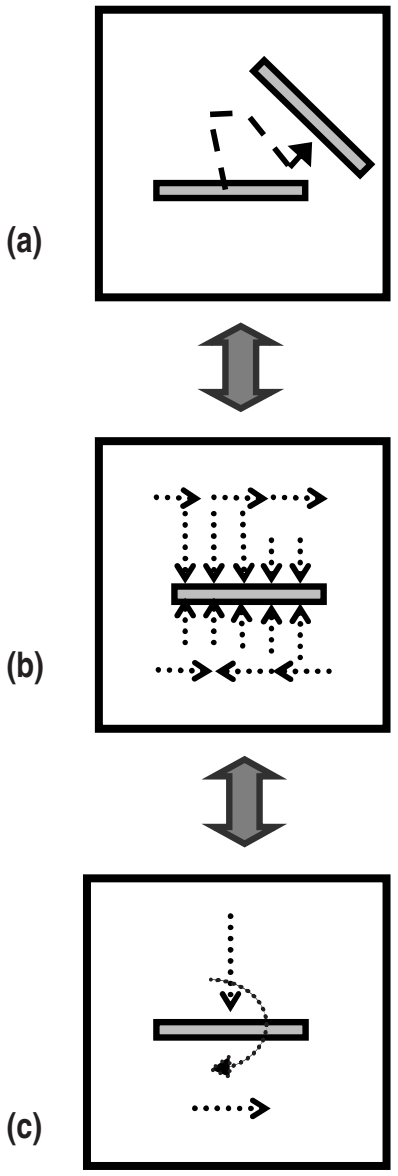

FIG. 3. Rigid-rod diffusion. The parallel, normal, and rotational diffusion of a rod segment (a) can be thought of as occurring due to point parallel and normal Brownian forces on the surface of the rod (b) and the moments resulting from the normal Brownian forces. In classical rigid-body mechanics, the effect of multiple point forces can be captured by a resultant force and resultant couple (c).

sion coefficients govern the variance of the sum of point normal and parallel forces, respectively, the corresponding variance should show a proportionality to the rod length similar to Eq. (16). Combining Eqs. (10) and (12) with Eq. (7), for two rods of length L^1 and L^2,

$$\frac{\langle F_i^1 F_i^1 \rangle}{\langle F_i^2 F_i^2 \rangle} = \frac{D_i'^2}{D_i'^1} = \frac{L^1}{L^2}, \quad i = p,n. \tag{17}$$

Equation (17) shows that the parallel and normal Brownian forces F_p and F_n, whose variance is governed by the diffusion coefficients, behave like the resultant forces of rigid-body mechanics. Similarly, if δf_n is a point normal Brownian force, and l is the variable indicating position along the rod length, then the variance of the net moment due to all δf_n on the rod surface can be written as

$$\begin{aligned}
&\left\langle \int_{-L/2}^{L/2} l \delta f_n dl \int_{-L/2}^{L/2} l' \delta f_n' dl' \right\rangle \\
&= \left\langle \int_{-L/2}^{L/2} dl \int_{-L/2}^{L/2} l \delta f_n l' \delta f_n' dl' \right\rangle = \left\langle \int_{-L/2}^{L/2} l \delta f_n l \delta f_n dl \right\rangle \\
&= \langle \delta f_n \delta f_n \rangle \int_{-L/2}^{L/2} l^2 dl = (4KT)(4\pi\eta)\frac{2L^3}{24} \\
&= (4KT)\frac{(\pi\eta L^3)}{3} = 4\frac{(KT)^2}{D_T}.
\end{aligned} \tag{18}$$

The third equality is because the point normal Brownian forces are random. The variance of the point normal force δf_n was obtained from Eqs. (12) and (16). From Eq. (18), it can be concluded that the variance of the net moment due to the point normal forces is determined by the rotational diffusion coefficient. A similar relation for the rotational diffusion coefficient has been derived in [15] in terms of the viscous forces. In Appendix A we show that our idealization of the Brownian forces as point normal and point parallel random forces, and the consequent idea that diffusion coefficients capture the distribution of their resultants, is physically consistent with classical mechanics theory.

B. Brownian force on a curved segment

By a treatment similar to that above, it can be shown that for a curved rod, the variance of the resultant of the Brownian point normal forces projected in a particular direction, is governed by the corresponding normal diffusion coefficient for the projected length in that direction (see Fig. 4). If δf_n is a point normal Brownian force acting at contour length l, and θ is the angle at that point, then the net projection of the point normal Brownian forces in the horizontal direction is

$$\begin{aligned}
&\left\langle \int_{-L/2}^{L/2} \delta f_n \cos\theta(l) dl \int_{-L/2}^{L/2} \delta f_n' \cos\theta(l') dl' \right\rangle \\
&= \left\langle \int_{-L_x/2}^{L_x/2} \delta f_n dl_x \int_{-L_x/2}^{L_x/2} \delta f_n' dl_x' \right\rangle = \langle \delta f_n \delta f_n \rangle L_x = \frac{4(KT)^2}{D_n'^X},
\end{aligned} \tag{19}$$

where $D_n'^X$ is the normal diffusion coefficient corresponding to the projected length L_x. The above relation can be proved similarly for the parallel Brownian forces. Also, the variance of the total moment due to projected normal forces can be shown governed by the rotational diffusion coefficient for the projected length. For a projection in the horizontal direction, the net moment due to normal Brownian forces is

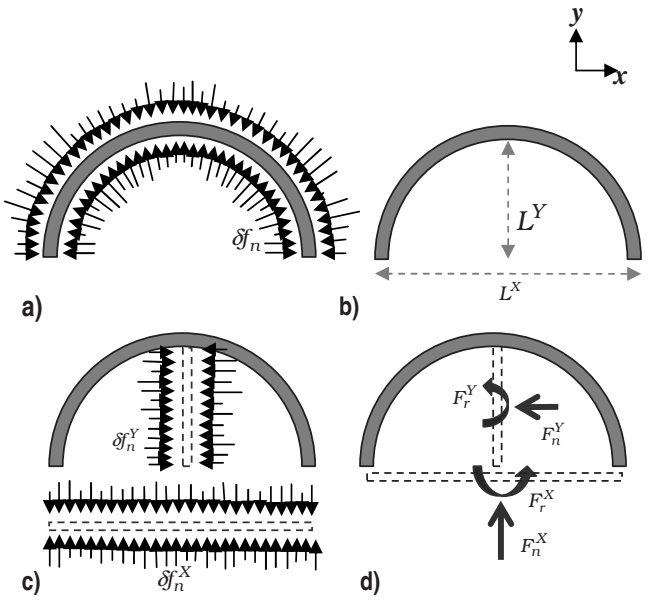

FIG. 4. Decomposition of normal forces on a curved segment into resultant forces and couples of the normal force projections in two mutually perpendicular directions. (a) Sample profile of point normal forces (δf_n) on a curved segment. (b) Projected lengths L_x and L_y of the curved segment in $-x$ and $-y$ directions. (c) Projections of the point normal forces in the $-x$ and $-y$ directions. δf_n^X is the x projection of the point normal force and δf_n^Y is the y projection of a point normal force. (d) Decomposition of the projected forces into resultant forces and couples. F_n^X and F_r^X are the resultant force and couple due to the point normal forces projected in the $-x$ direction. F_n^Y and F_r^Y are the resultant force and couple due to the point normal forces projected in the $-y$ direction.

$$\left\langle \int_{-L/2}^{L/2} l\delta f_n \cos^2\theta(l)dl \int_{-L/2}^{L/2} l\delta f_n' \cos^2\theta(l')dl' \right\rangle = \left\langle \int_{-L_x/2}^{L_x/2} \delta f_n l_x dl_x \int_{-L_x/2}^{L_x/2} \delta f_n' l_x' dl_x' \right\rangle = \langle \delta f_n \delta f_n \rangle \frac{L_x^3}{12} = \frac{4(KT)^2}{D_r'^X} \tag{20}$$

and $D_r'^X$ is the rotational diffusion coefficient corresponding to the projected length L_x.

C. Large-deflection Euler beam response to resultant forces and couples in mutually perpendicular directions

Consider the curved rod segment in Fig. 4, with N discrete point forces f_n^i acting normal to it at contour lengths l^i. Let θ^i be the segment angle at the points of action of the forces. According to large-strain Euler beam mechanics, the moment balance at $l=0$ due to the N discrete forces is

$$EI\frac{d\theta}{dl}(0) = \sum_{i=1}^{N} \left(f_n^i \cos\theta^i \int_0^{l^i} \cos\theta(l)dl \right) + \sum_{i=1}^{N} \left(f_n^i \sin\theta^i \int_0^{l^i} \sin\theta(l)dl \right), \tag{21}$$

where $\theta(l)$ is the segment angle as a function of contour length, and each integral captures the moment arm of the corresponding force component. Now, the above equation is difficult to solve, and has been solved only for simple loading conditions using elliptic integrals [27] and, iterative and numerical methods [28–33]. However, by resolving the normal forces over the segment $l=0-L$ into resultant forces and couples in two independently perpendicular directions [Fig. 4(d)], the moment balance for that segment can be accurately determined at $l=0$. In Fig. 4, if $-x$ and $-y$ are the axes along which the Brownian forces are resolved,[2]

$$EI\frac{d\theta}{dl}(0) = F_n^X\frac{L^X}{2} + F_n^Y\frac{L^Y}{2} + F_r^X + F_r^Y. \tag{22}$$

In Eq. (22), F_n^X and F_r^X are the resultant force and couple of the x projections of the point normal forces acting on the segment [Eqs. (23a) and (23b)], and F_n^Y and F_r^Y correspond to the y projections:

$$F_n^X = \sum_{i=1}^{N} f_n^i \cos\theta^i, \tag{23a}$$

$$F_r^X = \sum_{i=1}^{N} f_n^i \cos\theta^i \left(\int_0^{l_i} \cos\theta(l)dl - \frac{L^X}{2} \right). \tag{23b}$$

L^X and L^Y are the $-x$ and $-y$ projections of the segment length [Eqs. (23c) and (23d)], and are determined by numerical integration using a polynomial fit of $\theta(l)$ [see derivation for Eq. (30)],

$$L^X = \int \cos\theta(l)dl, \tag{23c}$$

$$L^Y = \int \sin\theta(l)dl. \tag{23d}$$

Note that Eq. (22) is dependent only on the resultant forces over the rod's projection, and does not require the exact profile of the normal forces on the rod.

When written only for a straight rod (y projection does not exist), Eq. (22) reduces to the standard moment-balance equation of Euler beam mechanics for a cantilever with a single force and couple at its center. If we represent a couple by equal and opposite forces at the ends of the segment, the generalized Euler beam moment-balance equation for a curved rod will appear as

$$EI\frac{d\theta}{dl}(l) = F_n^X\left(\frac{L^X}{2} - x\right) + F_n^Y\left(\frac{L^Y}{2} - y\right) + \frac{F_r^Y}{L^X}(L^X - x) + \frac{F_r^Y}{L^X}(L^Y - y). \tag{24}$$

Substitution of $l=0$, and therefore $x=y=0$, in the above equation gives back Eq. (22). The above equation can be

[2]To maintain the least correlation in the Brownian forces between the two projected directions, we always choose one direction to be along the line connecting the segment ends and the other direction to be perpendicular to it.

derived using the well-known free-body approach of solid mechanics. The moment at a point on a beam is determined by cutting a free surface at the point and calculating the moment required there to keep the resulting free body from rotating.

For a curved filament, the second differential of θ with respect to l can be obtained by distributing the differentiation of $d\theta/dl$ over the $-x$ and $-y$ projection,

$$EI\frac{d^2\theta(l)}{dl^2} = \frac{d}{dx}\left(EI\frac{d\theta(l)}{dl}\right)\frac{dx}{dl} + \frac{d}{dy}\left(EI\frac{d\theta(l)}{dl}\right)\frac{dy}{dl}. \quad (25)$$

At $l=0$, Eq. (25) can be correctly determined by noting that,

$$EI\frac{d}{dx}\frac{d\theta}{dl}(0) = -F_n^X, \quad (26a)$$

$$EI\frac{d}{dy}\frac{d\theta}{dl}(0) = -F_n^Y, \quad (26b)$$

$$\frac{dx}{dl}(0) = \cos\theta(0), \quad \frac{dy}{dl}(0) = \sin\theta(0). \quad (27)$$

There are two ways to show that Eqs. (26a) and (26b) are true. First, they can be directly obtained from Eq. (25) by differentiating with respect to x and y, setting x and y to zero, and adding in the remaining equal and opposite forces that exist at $x,y=0$ due to the couples F_r^X and F_r^Y. In Euler beam mechanics, $-EId^2\theta(l)/dl^2$ physically represents an internal shear force that acts perpendicular to the beam at the point l. Secondly, Eqs. (26a) and (26b) can be shown to be true for an arbitrary distribution of point normal forces f_n^i, as in the case of the curved rod depicted by Fig. 4 and Eq. (21). Consider stepping into the rod horizontally by an infinitesimal amount dx. At the new position, each vertical component of the point normal forces, $f_n^i \cos\theta^i$, has decreased its moment arm by dx. Noting that the horizontal force components do not contribute to the moment about the horizontal lever arm,

$$\frac{d}{dx}\left(EI\frac{d\theta}{dl}(0)\right) = \frac{EI\frac{d\theta}{dl}(0+dx) - EI\frac{d\theta}{dl}(0)}{dx} = \frac{\sum_{i=1}^{N} f_n^i \cos\theta^i\left[\int_0^{l^i}\cos\theta(l)dl - dx\right] - \sum_{i=1}^{N} f_n^i\cos\theta^i\int_0^{l^i}\cos\theta(l)dl}{dx}$$

$$= \frac{-\left(\sum_{i=1}^{N} f_n^i\cos\theta^i\right)dx}{dx} = -F_n^X. \quad (28)$$

Finally, the difference between the end angles of the segment can be determined by integrating $d\theta/dl$. Integration of Eq. (24) between $l=0$ and L gives

$$\theta(0) - \theta(L) = \frac{1}{EI}\left(F_n^X\frac{L_Y^2}{8} + F_n^Y\frac{L_Y^2}{8} + F_r^X\frac{L^X}{2} + F_r^Y\frac{L^Y}{2}\right). \quad (29)$$

Note that the integration of the internal moment, $EI\,d\theta/dl$, requires knowledge of the exact distribution of the point normal forces on the segment. However, Eq. (29) was derived assuming the moment distribution due to a single resultant force and couple. The resulting error is discussed toward the end of this section.

In all, there are six equations that can be solved to obtain the large-deflection Euler beam response of a curved rod segment under resultant forces and couples: an equation for moment balance [Eq. (22)]; two equations of force balance [Eqs. (26a) and (26b)]; an equation of angle change [Eq. (29)]; and two equations for the segment length projections [Eqs. (23c) and (23d)]. The six equations, solved simultaneously with boundary conditions on $l=L$, give the values of $d\theta/dl$, $(d/dx)(d\theta/dl)$, $(d/dy)(d\theta/dl)$, θ, x, y at $l=0$. The configuration of the segment is obtained from a fifth-order polynomial approximation of $\theta(l)$ determined as

$$\theta(l) = \theta(0) + \sum_{n=1}^{5}\varphi_n l^n, \quad (30)$$

where the coefficients φ_n are obtained by fitting Eq. (30) for $\theta(L)$, $(d\theta/dl)(0)$, $(d\theta/dl)(L)$, $(d^2\theta/dl^2)(0)$, $(d^2\theta/dl^2)(L)$.

In the above scheme for solving large-deflection beam mechanics, error arises from two places: (1) from the determination of $\theta(0)$ in Eq. (29) since the integration is sensitive to the profile of the normal forces along the moment-arm; (2) from the fifth-order approximation of $\theta(l)$ which in turn affects the estimates for L^X and L^Y [Eqs. (23c) and (23d)]. However, as shown below, we solve the above equations at segments within a beam/filament, instead of over the entire beam/filament; and by stipulating the segment lengths to be much smaller than the persistence length, we improve the accuracy of the formulation greatly (see Sec. III).

D. Brownian fluctuation of a semiflexible filament

In the previous section we showed how Euler beam mechanics can be solved on a segment with relative ease, provided the resultants of Brownian force projections in two

mutually perpendicular directions are known. We also showed that the resultant Brownian forces can be obtained by random sampling of Gaussian distributions whose variances are determined by the diffusion coefficients for the projected lengths. In this section, we put it all together and solve for the Brownian fluctuation dynamics of semiflexible filament. We divide the filament into segments, determine the Brownian forces on each segment, and solve a modified version of the above Euler beam equations over all segments simultaneously to balance the Brownian and other forces on each. By way of nomenclature, we denote a segment and the variables associated with it by uppercase letters, and we denote a node (segment intersection) and the variables associated with it by lowercase letters. A segment I is always flanked by node i on the left and node $i+1$ on the right.

Figure 5 shows the forces and couples on a segment which has been cut off from a semiflexible filament in Brownian fluctuation. There are three kinds of forces and couples at play.

(1) Brownian forces and couples: The normal Brownian forces and their role in the bending of a segment have been discussed above. The parallel Brownian forces which affect segment translation and may contribute to moments elsewhere in a curved filament need to be included in the force balance also.

(2) Forces and couples at the segment interface: When a segment it cut from a filament, a remnant force (V) and a couple arise at the cut interface from any internal bending or stretch mechanics there, from any force or couple exerted by the neighboring segments, and from any force or couple applied externally at the filament ends.

(3) Viscous forces or couples: The viscous forces resisting parallel or normal motion and the viscous moments resisting rotational motion can be calculated directly from the segment deformation in a time interval by straightforward numerical integration (Appendix B).

As discussed earlier, the Brownian forces are determined from Gaussian distributions with variance determined by the diffusion coefficients. We note at this point that the variance as described in Eq. (15) is for the Brownian force at a time point t. The variance for the net Brownian force in a time interval Δt is given as

$$\langle F_i F_i \rangle = 4\frac{(KT)^2}{D_i'}\Delta t. \tag{31}$$

The above equation is obtained by integrating the forces in Eq. (15) over Δt and applying arguments similar to Eq. (16) or (19). We also note that the diffusion coefficient in Eq. (31) is calculated from the segment configuration at the beginning of Δt. This is in keeping with the way the parallel and normal displacements of a rod are measured in a time interval in order to determine diffusion coefficients—the parallel and normal directions are determined with respect to the rod orientation at the beginning of the time interval. Consequently, in the framework of a forward Euler time-stepping procedure, D_i' and therefore the Brownian forces F_i appear as constants in the balance equations for each time step. On the other hand, the viscous forces and the forces arising at the cut interface are functions of the segment or filament deformation in each time step and are iteratively updated. Shown below are the six balance equations assembled for each segment I [Eqs. (32)–(37)]. All segment equations, along with

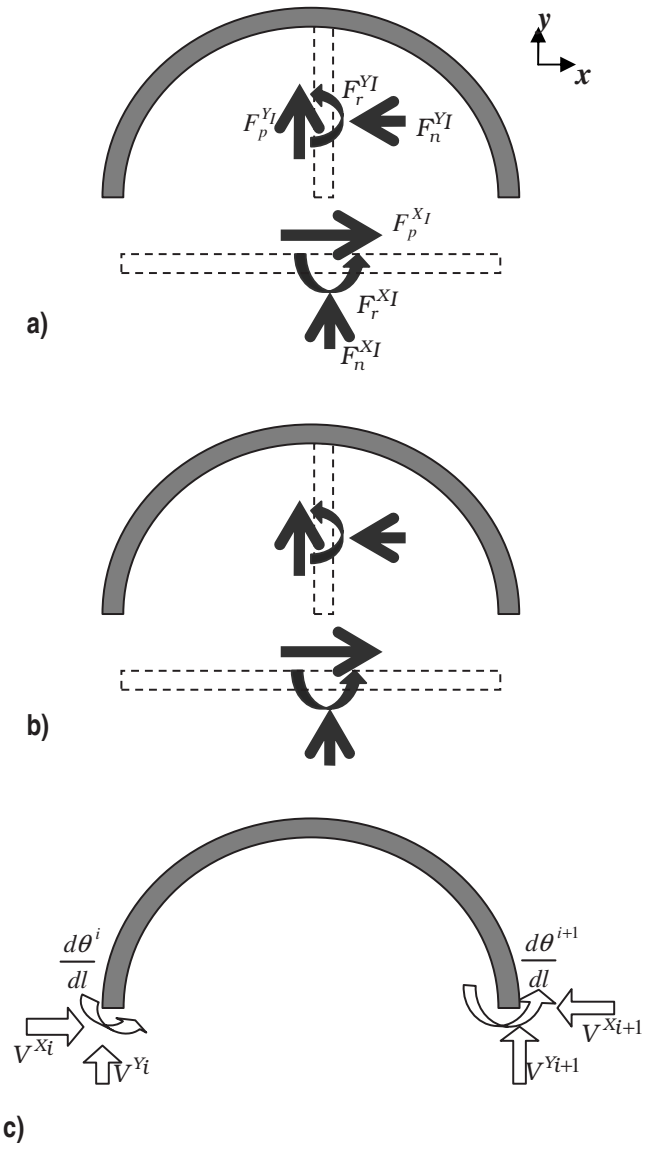

FIG. 5. Forces on segment I (gray rod) of a fluctuating semiflexible filament. (a) Brownian forces: The parallel and normal Brownian forces projected in the $-x$ and $-y$ directions (white rods) are resolved into the corresponding resultant forces and couples. The Brownian force resultants (F) are written with superscripts indicating the direction of projection and segment number, and with subscripts indicating the kind of force (parallel, normal, or rotational). It should be noted that the rotational force is a couple which captures the net moment of the projections of the normal Brownian forces about the center of the projection length. (b) Viscous forces: The viscous forces arise from the frictional resistance to motion. (c) Forces at cut surface: Forces (V) and couples ($d\theta/dl$) latent at the cut surfaces (nodes i and $i+1$), arising either from the internal resistance to bending, or from the forces and couples transmitted by neighboring segments, or from the forces and couples imposed at the boundary. The lower-case superscripts indicate the node number associated with the force or couple.

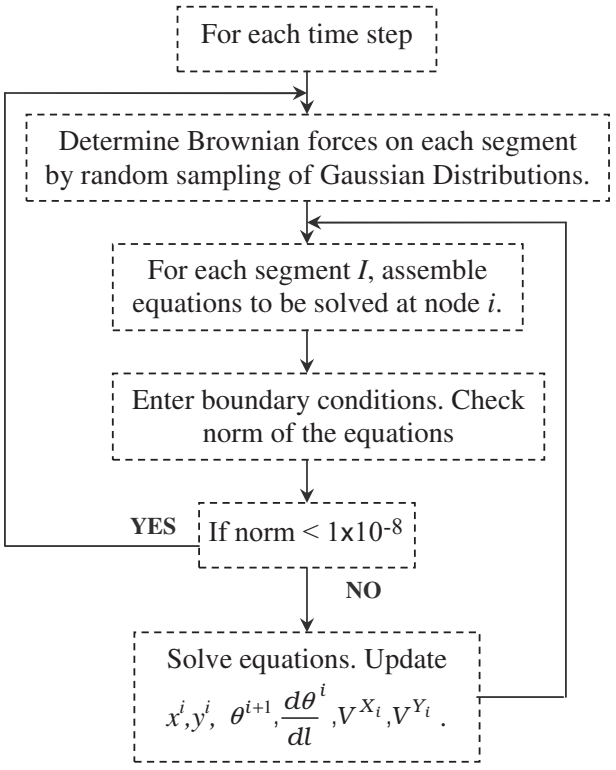

FIG. 6. Schematic of the solution process.

boundary conditions, are solved simultaneously in each time step, to update the values of x, y, θ, $d\theta/dl$, V^X, and V^Y at each ith node for the end of that time step. The contribution of the viscous drag to the change in filament end angles, to the balance of moment, and to the balance of forces in the x and y directions, are shown as ψ_θ, ψ_C, ψ_V^X, and ψ_V^Y, respectively, in Eqs. (34)–(37). The full expression for these terms is discussed in Appendix B. Figure 6 shows the schematic of the solution process.

$$x^i - x^{i+1} = -\int_0^{L^I} \cos[\theta(l)]dl, \tag{32}$$

$$y^i - y^{i+1} = -\int_0^{L^I} \sin[\theta(l)]dl, \tag{33}$$

$$\theta^i - \theta^{i+1} = \frac{1}{EI}\left(F_n^{X_I}\frac{L^{X_I}{}^2}{8} + F_n^{Y_I}\frac{L^{Y_I}{}^2}{8} + F_r^{X_I}\frac{L^{X_I}}{2} + F_r^{Y_I}\frac{L^{Y_I}}{2} + V^{X_{i+1}}\frac{L^{X_I}{}^2}{2} + V^{Y_{i+1}}\frac{L^{Y_I}{}^2}{2} + L\left.\frac{\partial\theta}{\partial l}\right|^{i+1} + \Psi_\theta^I\right), \tag{34}$$

$$\left.\frac{\partial\theta}{\partial l}\right|^i - \left.\frac{\partial\theta}{\partial l}\right|^{i+1} = \frac{1}{EI}\left(F_n^{X_I}\frac{L^{X_I}}{2} + F_n^{Y_I}\frac{L^{Y_I}}{2} + F_r^{X_I} + F_r^{Y_I} + V^{X_{i+1}}L^{X_I} + V^{Y_{i+1}}L^{Y_I} + \Psi_C^I\right), \tag{35}$$

$$V^{X_i} - V^{X_{i+1}} = \frac{1}{EI}(F_n^{Y_I} + F_p^{X_I} + \Psi_V^{X_I}), \tag{36}$$

$$V^{Y_i} - V^{Y_{i+1}} = \frac{1}{EI}(F_n^{X_I} + F_p^{Y_I} + \Psi_V^{Y_I}), \tag{37}$$

where

$$\theta(l) = \theta^i + \sum_{n=1}^{5} \varphi_n l^n, \tag{38}$$

$$\varphi_n = f\left(\theta^{i+1}, \frac{d\theta_i}{dl}, \frac{d\theta}{dl}_{i+1}, \frac{d^2\theta_i}{dl^2}, \frac{d^2\theta}{dl^2}_{i+1}\right), \tag{39}$$

$$\left.\frac{d^2\theta}{dl^2}\right|^i = -\frac{1}{EI}[F_n^{X_I}\cos(\theta^i) + F_n^{Y_I}\sin(\theta^i)]. \tag{40}$$

Note that Eqs. (36) and (37) are force-balance equations that include both bending and translational forces. Consequently, the end force V^i balances both bending and translational forces.[3] However, as discussed in Sec. II C, $EI(d^2\theta/dl^2)(l)$ physically represents the internal shear force perpendicular to the segment at l, which balances bending forces only. Therefore, Eqs. (36) and (37) cannot be used to determine the components of $d^2\theta/dl^2$ as in Eqs. (26a) and (26b) of Sec. II C. Instead, the components of $d^2\theta/dl^2$ at the ith node are determined directly from the solution of each iteration [Eq. (40)], and are used to obtain the fifth-order polynomial approximation of $\theta(l)$ for the next iteration [Eqs. (38) and (39)].

III. RESULTS AND VALIDATION

We validate our model for a range of Brownian phenomena in which the filament strain energy is the principal resistance to thermal motion. The filament properties and simulation details for each case are shown in Table I. For the flexible filaments, we chose the simulation time to be much larger than the relaxation time of the largest bending mode of interest and the time intervals to be smaller than the relaxation time for the smallest bending mode of interest. From a preliminary estimate of the number of segments required to give less than 1×10^{-6} error in the deflections of a unit cantilever (Sec. III B 1), we chose the number of segments so that every 5° angle change is resolved by at least two segments.

[3]Note that any Euler bucklinglike force imposed via V is naturally solved in Eq. (35). The following point about the projected directions should also be noted. As mentioned earlier, to obtain the least correlation in the Brownian forces between the two projected directions, we always choose one direction to be along the line connecting the segment ends and the other direction to be perpendicular to it. This entails rotating the frame of reference for each segment. Therefore a rotational correction is applied on the nodal variables θ_i and V_i which communicate between segments. However, for clarity of expression, the rotational corrections are not shown in Eqs. (32)–(40).

TABLE I. Boundary conditions for freely diffusing and cantilevered filaments. Since six equations or degrees of freedom are solved for each filament segment, six boundary conditions are required.

	Freely diffusing	Cantilevered
1	$\left.\frac{d\theta}{dl}\right\|_{L=0}=0$	$x\|_{L=0}=0$
2	$V^X\|_{L=0}=0$	$y\|_{L=0}=0$
3	$V^Y\|_{L=0}=0$	$\theta\|_{L=0}=0$
4	$\left.\frac{d\theta}{dl}\right\|_{L=L_f}=0$	$\frac{d\theta}{dl}\|_{L=L_f}=0$
5	$V^X\|_{L=L_f}=0$	$V^X\|_{L=L_f}=0$
6	$V^Y\|_{L=L_f}=0$	$V^Y\|_{L=L_f}=0$

A. Rigid filament dynamics

1. Free diffusion of a straight filament

At high flexural rigidity, the diffusion coefficient of a freely diffusing semiflexible filament should match the diffusion coefficient of a rigid rod of the same length [Eqs. (11)–(13)]. We simulated the free diffusion of semiflexible filaments for lengths ranging from 1 to 5 μm and calculated the tangential, normal, and rotational diffusion coefficients from the net displacements in each time interval [Eq. (14)]. We also verified that there was no dependence on the number of segments, by repeating the simulations for 1, 5, and 20 segments each. The boundary conditions for free diffusion are listed in Table I and the simulation details for each run in Table II. Shown in Fig. 7 are the average and standard deviation of eight simulation runs for each data point. The simulated diffusion coefficients showed the same dependence on filament length as the diffusion coefficient of rigid rods [Eqs. (11)–(13)], irrespective of the number of segments used.

B. Semirigid filament dynamics

In Sec. III B 1, we validate the proposed methodology for solving large-deflection Euler beam mechanics. In Sec. III B 2, we validate our filament model in the small-fluctuation or semirigid regime by showing that, for a test case of a cantilevered condensed chromosome, the analytical predictions for angular and transverse thermal fluctuations are recovered, irrespective of the viscosity of the medium.

1. Large-deflection cantilever bending

We compared the deflections of a simulated cantilever against published data for various weight loadings [32], and for various vertical end loadings [30] [Fig. 8(a)]. Weight loading was simulated by applying over each segment the numerical estimate of the resultant force and couple on it due to its weight. End loading was simulated by setting the load as the boundary condition for V_y at the free end (see Table II). As shown in Figs. 8(b) and 8(c), for both loading cases, the vertical (Δy), horizontal (Δx), and angular ($\Delta\theta$) deflections of a simulated cantilever matched published results. We also simulated an experimental loading of a cantilever ruler under its own weight (0.554 N) and a vertical end load of 3.92 N [33]. The length and flexural rigidity of the ruler were 30 cm and 0.24 N m^2, respectively. As shown in Fig. 8(d), the simulated deflection profile matched the experimental profile correctly.

2. Transverse Brownian fluctuation of cantilevered chromosome

In the semirigid regime ($L_p/L \gg 1$), the thermal fluctuations of a filament are small, and analytical expressions can be derived for the angular and transverse fluctuations of the filament in a cantilevered state. For one, the histogram of angular fluctuations matches the Boltzmann distribution [see Eq. (2)],

$$p(\Delta\theta) = \frac{1}{\sqrt{2\pi\langle\Delta\theta^2\rangle}} \exp\left(-\frac{(\Delta\theta)^2}{2\langle\Delta\theta^2\rangle}\right) \tag{41}$$

with variance given as

TABLE II. Filament and simulation details for validation studies of Sec. III.

	Rigid filament (Sec. III A 1)	Cantilevered chromosome (Sec. III B 2)	Freely diffusing F-actin-phalloidin [36] (Sec. III C 1)
Filament flexural rigidity EI	1×10^{-6} N m^{2a}	5.523×10^{-23} N m^2	7.3×10^{-26} N m^2
Filament diameter d	8×10^{-2} μ m^2	0.8 μm	0.008 μm
Filament length L	1–5 μm	5 μm	15.5 μm
L_p/L	$>10^{-10}$	2694.1	1.14
No. of segments	1–20	25	62
Simulation time	200 s	20 s	80 s
Simulation time interval	0.001 s	0.0002/0.002 s	0.01 s
Temperature	20 °C	25 °C	25 °C
Viscosity	1×10^{-3} Pa s	$0.89\times10^{-3}/0.89\times10^{-1}$ Pa-s	0.89×10^{-3} Pa s

[a]Arbitrarily large EI.

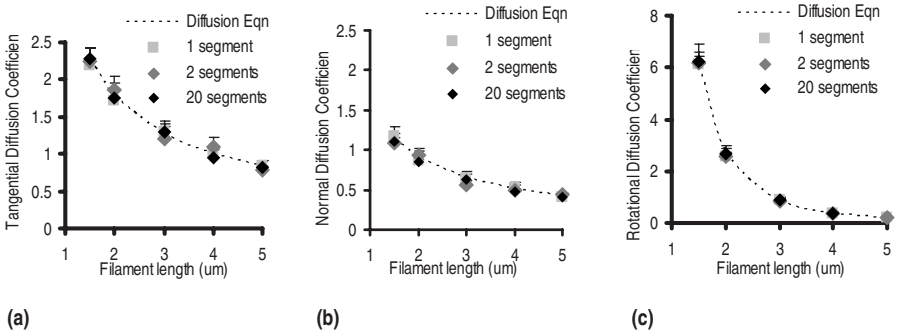

FIG. 7. Rigid limit: Free diffusion of rigid rods. At high flexural rigidity, the tangential (parallel), normal, and rotational diffusion coefficients of semiflexible filaments of different lengths (1–5 μm) matched that of rigid cylindrical rods given by Eqs. (11)–(13) (shown as a broken line). This was irrespective of the number of segments used to simulate the filament (shown for 1, 5, and 20 segments). Each average simulated diffusion coefficient was determined from eight simulation runs, with the details of a run shown in Table II.

$$\langle \theta^2 \rangle = \frac{KTL}{EI}. \tag{42}$$

For the small fluctuations, the mean square of the transverse fluctuation (Δy) along the filament contour can be derived by equating the energy of each bending mode to $KT/2$ (equipartition theorem), and it can be shown to have a cubic dependence on contour length [34],

$$\langle \Delta y^2 \rangle = \frac{32KTl^3}{\pi^4 EI}. \tag{43}$$

We examined our model in the semirigid regime by simulating the cantilevered thermal fluctuations of a 5 μm condensed chromosome and comparing against the experimental study by Poirier *et al.* [35]. Due to the large EI and diameter (see Table II), the thermal fluctuations of the chromosomes are small, and were found to agree with the analytical predictions for a fluctuating uniform elastic cantilever, implying such a microstructure [35]. We initially did our simulations in water at 25 °C, with the EI of 5.56×10^{-23} N m^2 estimated in [35]. Figure 9(a) shows the normalized histogram of the angular fluctuations of the free end of the simulated chromosome. The distribution closely matched the predicted Boltzmann distribution [Eq. (41)] for the corresponding variance [Eq. (42)]. Also, the mean-square transverse fluctuations along the filament length showed the cubic dependence on filament length predicted by Eq. (43) [Fig. 9(b)]. The time profile of thermal fluctuations in Fig. 9(c), however, suggested a smaller relaxation time than that observed in the experiments (Fig. 4a in [35]). A preliminary calculation of the relaxation time gave an estimate of 0.14 s for chromosome fluctuations in water [36], which was on the order of that observed in the simulations. Since the experimental observations were performed within a colchicine-arrested cell, and assuming cytoskeletal viscosity to be at least 100 times greater than that of water [2,37], we repeated the simulation of chromosome fluctuation in a "cell-like" medium with 100 times the viscosity of water. The results for these simulations are shown in Figs. 9(d)–9(f). The new time profile of the angular fluctuations showed an increase in the bending relaxation times [Fig. 9(f)], and was similar to that observed in the experiments (Fig. 4a of [35]). Importantly, however, the distribution of angular and transverse fluctuations [Figs. 9(d) and 9(e)] did not change with the change in viscosity, as predicted by the dependencies in Eqs. (41) and (43). These results validate the ability of the model to capture the interplay between Brownian, viscous, and bending forces in the small-fluctuation or semirigid limit.

C. Semiflexible filament dynamics

1. Brownian fluctuation of freely diffusing F-actin-phalloidin

We validated our model in the semiflexible limit ($L_p/L \approx 1$) by comparing the simulated thermal fluctuations of a phalloidin-labeled actin filament against the experimental observations of Gittes *et al.* [36]. The filament length and EI are 15.5 μm and 7.3×10^{-26} N m^2.

Figure 10(a) shows frames of the Brownian simulation of the actin filament, 1.5 s apart. The filament conformations in Fig. 10(a) are similar to those observed by Gittes *et al.* [36]. There are either filaments with smoothly bending conformation (constant or gradually changing curvature) or filaments with long regions of nearly constant and small curvature separated by a short region of high curvature or bends. In experiments, due to the Gaussian blurring, some bends appear as sharp kinks that were initially attributed to internal defects in the filament [38–40]. In Fig. 10(b) we show two filament conformations that resemble ones observed by Gittes *et al.* [36] and Kas *et al.* [39]. The inset shows the filaments plotted with large symbols to imitate Gaussian blurring, and sharp kinks are evident. However, the plain filament contour alongside show the sharp kink as regions of high curvature separating regions of monotonic low curvature.

Some average quantifications of the filament bending can be compared against theoretical predictions. The average decay in angle correlation along the filament contour is given by Eq. (4), and the simulation was found to match it [Fig. 10(c)]. The worm model predicts the mean-square end-to-end distance $\langle R^2 \rangle$ for the freely fluctuating filament in 2D to be 208.7 μm^2, from the following equation [2]:

$$\langle R^2 \rangle = 8L_p^2 \left[\exp\left(-\frac{L}{2L_p} \right) - 1 + \frac{L}{2L_p} \right]. \tag{44}$$

The corresponding $\langle R^2 \rangle$ from our simulations was 210.7 μm^2. Finally, the different independent bending modes

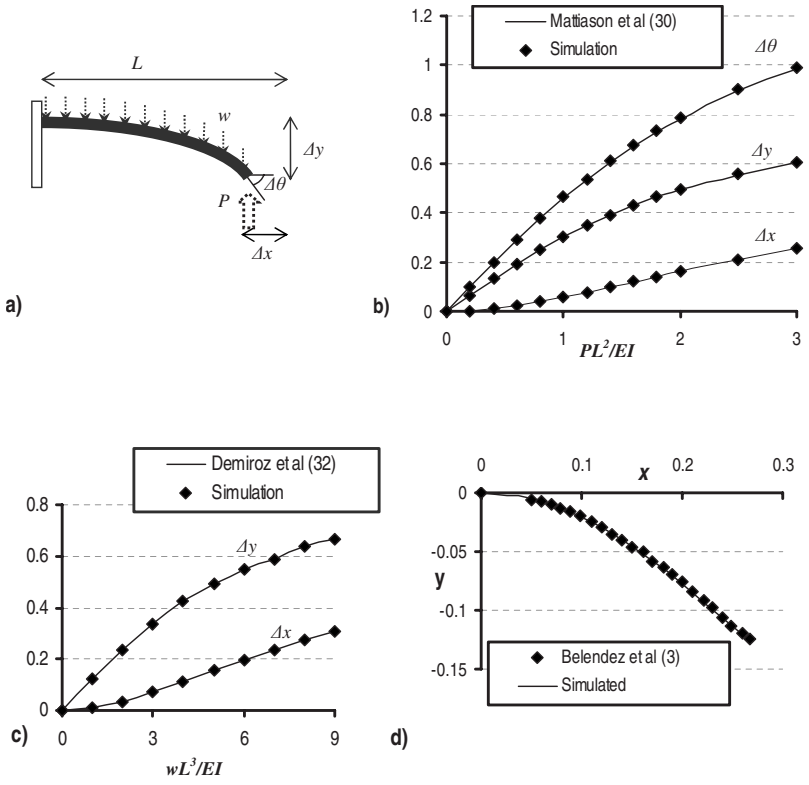

FIG. 8. Validation of proposed large-deflection Euler beam equations. (a) Cantilever under weight (w) and vertical end loading (P). (b) $-x$, $-y$ deflections and end angle of a cantilever under different vertical end loading (P). The end loadings are scaled by the filament length (L) and flexural rigidity (EI), and the deflections are scaled by the filament length. The simulated cantilever deflections matched that calculated by Mattiason *et al.* [30]. (c) $-x$ and $-y$ deflections of a cantilever under different weight loading. The weight loading is scaled by the filament length (L) and flexural rigidity (EI), and the deflections are scaled by the filament length. The simulated cantilever deflections matched that calculated by Demiroz *et al.* [32]. (d) Simulation of the experimental loading of a ruler under its own weight (0.224 N) and a vertical end load of 0.394 N. The length and flexural rigidity of the ruler were 3 cm and 0.24 N m^2, respectively. The $-x$ and $-y$ profiles of the simulated cantilever matched those of Belendez *et al.* [33].

for the filament can be extracted by decomposing the filament angle along its contour into a Fourier series [36,40],

$$\theta(l) = \sqrt{\frac{2}{L}} \sum_{n=0}^{\infty} a_n \cos\left(\frac{n\pi}{L} l\right). \tag{45}$$

In the above equation, the Fourier coefficient a_n is the amplitude of the nth bending mode. By equating the net bending energy from each mode to $KT/2$ (equipartition theorem), the variance of the bending amplitudes can be obtained for each mode as [36]

$$\langle a_n^2 \rangle = \frac{KT}{EI} \left(\frac{L}{n\pi}\right)^2. \tag{46}$$

Figure 10(d) shows that the variance of the bending amplitudes measured from an 80 s simulation using Eq. (45). It closely matches the values predicted by Eq. (46). The largest bending mode was underestimated due to its large relaxation time (about 15 s) and the consequently large simulation or experiment time required to obtain a statistically relevant sampling of the bending amplitudes [36,40]. For the second bending mode, we show in Fig. 10(d) that the relaxation profile matches that calculated by Brangwynne *et al.* [38].

IV. DISCUSSION

In this paper, we presented an idealization of semiflexible filaments as a string of continuously flexible rods. The idealization allows for overcoming many of the discretization errors and computational costs that come with simulating semiflexible filament dynamics by traditional idealizations such as the string of beads. We first showed how the Brownian forces over the flexible rods and the resulting Euler beam mechanics can be determined. Brownian forces due to solvent collision were considered as point normal and parallel forces acting on the surface of the rods. The projections of the point Brownian forces in two mutually perpendicular directions were resolved into resultant forces and couples. The diffusion coefficients for each projected length of the rod were then shown to govern the distribution of the Brownian resultant forces and couples over that projected length. On the other hand, by projecting the Brownian forces in two mutually perpendicular directions, we showed that the Euler moment over the curved rod can be correctly determined, and the large-deflection Euler beam mechanics can be solved to fifth-order continuity within the rod. Finally, working off these arguments, we solved for the Brownian fluctuation dynamics of semiflexible filaments: by dividing the filament into segments much smaller than the persistence length, imposing the Brownian force resultants on each segment, and simultaneously solving for the Euler beam mechanics in all segments. The immediate benefits of such an approach were (1) a reduction in computational cost that came with discretizing into rods as opposed to spheres, (2) an improved accuracy in capturing filament shape that came with using higher-order continuity for contour angles, and (3) the natural preserving of filament inextensibility that came with solving large-deflection beam mechanics. We found that the approach was physically consistent in that the translational, rotational, and bending Brownian dynamics of filaments can be captured from the rigid to the semiflexible limit.

The key departure of our approach from other modeling techniques was the discretization into rod segments. It allowed us to directly apply the diffusion coefficients and the bending mechanics well established for cylindrical rods, and

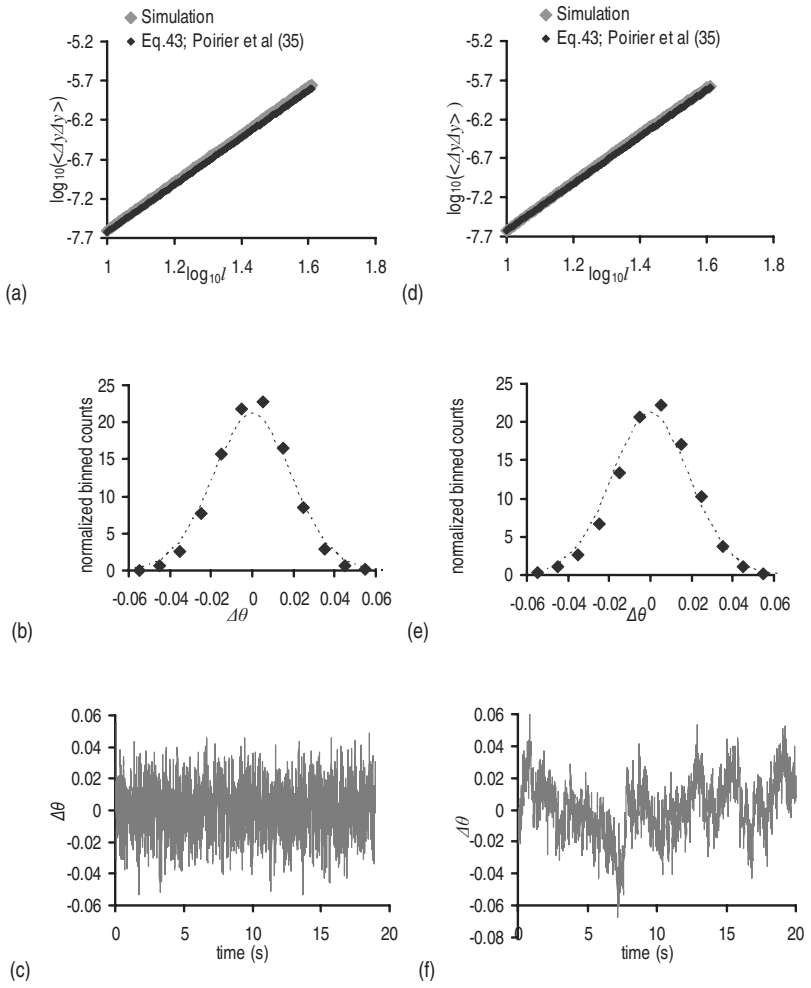

FIG. 9. Validation of model in semirigid regime by comparison against the thermal fluctuations of a cantilevered condensed chromosome in Poirier *et al.* [35]. (a) Transverse fluctuations of a cantilevered condensed chromosome in water: The transverse fluctuations [Δy in Fig. 8(a)] show a cubic dependence on cantilever length as expected for small thermal fluctuations [Eq. (43)]. (b) Angular fluctuations of a cantilevered condensed chromosome in water: The figure shows the normalized binned counts of the angular fluctuation [$\Delta\theta$ in Fig. 8(a)] of a cantilevered condensed chromosome. The plot matches the binned counts of a Boltzmann distribution of corresponding variance [Eqs. (41) and (42)]. (c) Time profile of angular fluctuations of a cantilevered condensed chromosome in water: The time profile of the angular fluctuations [$\Delta\theta$ in Fig. 8(a)] is plotted at 0.01 s intervals. The relaxation time of the fluctuations is much faster than that shown in Poirier *et al.* [35]. The observations in [35] were made within a colchicine-arrested cell, whereas these simulations (Figs. 9(a)–9(c)) were performed in water at 25 °C. (d) The transverse fluctuations of a cantilevered condensed chromosome in cell: The transverse fluctuations retained the cubic dependence on cantilever length as expected for small thermal fluctuations [Eq. (43)], irrespective of the viscosity of the medium. The simulation was performed in a cell medium, with 100 times the viscosity of water at 25 °C. (e) Angular fluctuations of a cantilevered condensed chromosome in cell: The distribution of the angular fluctuation of the cantilevered chromosome was similar to the Boltzmann distribution of corresponding variance [Eqs. (41) and (42)], and was independent of the viscosity of the medium. The simulation was performed in a cell medium, with 100 times the viscosity of water at 25 °C. (f) Time profile of angular fluctuations of a cantilevered condensed chromosome in cell: The cell medium was assumed to have 100 times the viscosity of water at at 25 °C. The profile is plotted in 0.01 s intervals. The relaxation time of the large-wavelength fluctuations is longer than that observed in, and closer to that observed in Poirier *et al.* [35].

avoid the hydrodynamic complexities associated with approximating a filament into a string of beads. A bead-string model by Alberto *et al.* [22] also used the parallel and normal friction coefficients of a cylindrical rod as the anisotropic friction coefficients of a bead. They were able to reproduce the relaxation dynamics of rigid filaments and the tangent-angle decay of semiflexible filaments. However, in our method we can include information on the rotational diffusion coefficient of a rod in a physically consistent manner, as the moment of the normal Brownian forces. This allows us to capture the effect of the Brownian force over a much larger length scale than a single bead. However, a deficiency in our model is that it does not account for the hydrodynamic interaction between the rod segments of a filament. This issue is addressed in other work [41].

The proposed model is particularly applicable in the semiflexible limit, where the filament aspect ratio is large and end-factor corrections for diffusion coefficients can be ne-

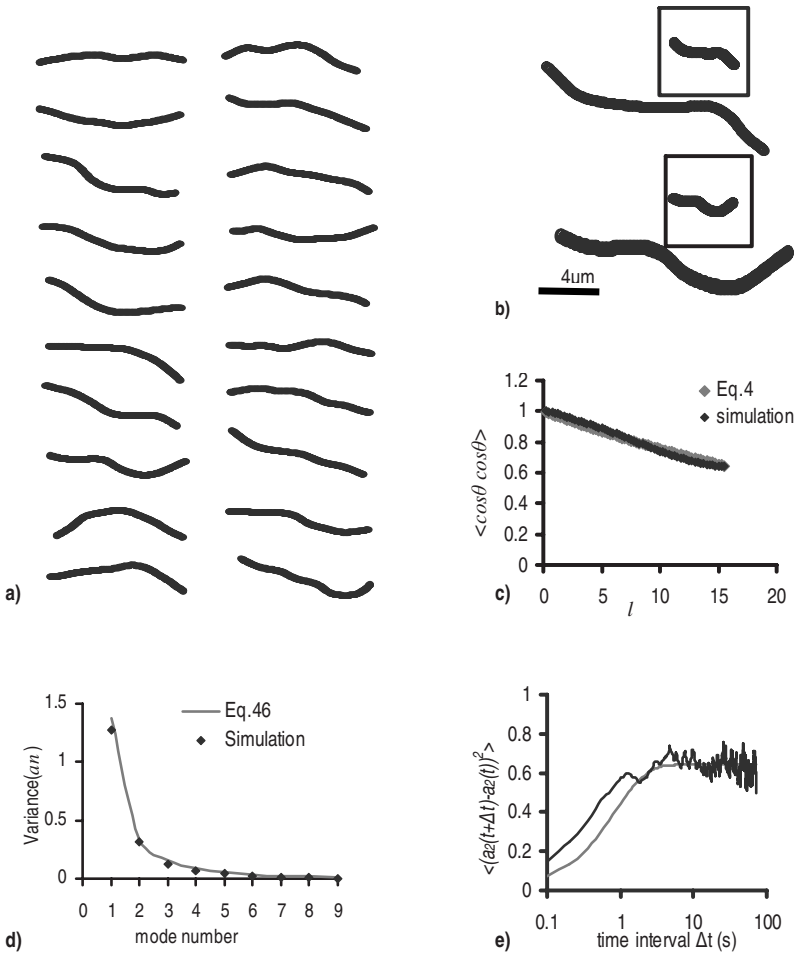

FIG. 10. Semi flexible filament dynamics. (a) Time-lapse images of simulated actin filaments in a thin film of water at 25 °C. The sequence of images, 1.5 s apart, run top to bottom and left to right. The filament is 15.5 μm long. (b) Simulated images of sharp bends in actin filaments (insets) are similar to those observed in Kas *et al.* [39] (top) and Gittes *et al.* [36] (bottom). The images were plotted with large symbols to imitate Gaussian blurring, which creates the impression of sharp bends or kinks. The enlarged images show the corresponding contour of the filament within the inset. (c) Correlation of contour angle along contour length: The decay in the cosine angle correlation along the filament contour follows that specified by the worm model [Eq. (4)] for a persistence length of 17.7 μm. (d) Variance of bending modes: The variance of the amplitudes (a_n) of the different bending modes follows that specified by Eq. (46) requiring each independent bending mode to have an energy $KT/2$ (equipartition theorem). (e) Time relaxation of second bending mode: The relaxation time profile of the second bending mode (black dots) matches the theoretical approximation of Brangwynne *et al.* [38] (gray line).

glected, and where the shape fluctuations are small so that coarse discretizations are sufficient to resolve Brownian forces and Euler mechanics. This opens up possibilities for modeling the mechanics of cytoskeletal networks where the filament length and fluctuation between cross links are typically small. The consequent saving in discretization allows for modeling larger and more realistic networks.

ACKNOWLEDGMENTS

The authors are thankful to members of Molecular Cell Biomechanics Laboratory for their invaluable input. Financial suport form National Science Foundation is gratefully acknowledged.

APPENDIX A

A basic tenet in the classical theory of rigid-body mechanics is as follows: for a rigid rod divided into segments, with the resultant force and couple known for each segment, the net moment on the rod is given by sum of the segment couples and the moments of the resultant forces at the segments. We show that the tenet holds for Brownian forces; i.e., for a rigid rod in Brownian diffusion, with the variance of the resultant normal force (f_n) and resultant couple (f_r) for each segment known from its diffusion coefficients, the variance of the net rod moment, F_r, is equal to the sum of the variance of the resultant couples and the variance of the moments of the resultant forces at the segments.

First we note that

$$\int_{-L/2}^{L/2} l^2 dl = \sum_{-N/2}^{N/2} \left((n\Delta L)^2 \Delta L + \int_{n\Delta L-\Delta L/2}^{n\Delta L+\Delta L/2} l^2 dl \right). \quad \text{(A1)}$$

Second, from Eq. (18), the variance of the net moment on the rigid rod can be written as

$$\langle F_r F_r \rangle = \langle \delta f_n \delta f_n \rangle \int_{-L/2}^{L/2} l^2 dl. \quad \text{(A2)}$$

Combining Eqs. (A1) and (A2)

$$\begin{aligned} \langle F_r F_r \rangle &= \langle \delta f_n \delta f_n \rangle \sum_{-N/2}^{N/2} (n\Delta L)^2 \Delta L + \langle \delta f_n \delta f_n \rangle \sum_{-N/2}^{N/2} \int_{n\Delta L-\Delta L/2}^{n\Delta L+\Delta L/2} l^2 dl \\ &= \frac{\langle f_n f_n \rangle}{\Delta L} \sum_{-N/2}^{N/2} (n\Delta L)^2 \Delta L + \sum_{-N/2}^{N/2} \langle \delta f_n \delta f_n \rangle \int_{n\Delta L-\Delta L/2}^{n\Delta L+\Delta L/2} l^2 dl \\ &= \sum_{-N/2}^{N/2} (n\Delta L f_n n\Delta f_n) + \sum_{-N/2}^{N/2} \langle f_r f_r \rangle. \end{aligned} \quad \text{(A3)}$$

APPENDIX B

Let v_n and v_p be the normal and parallel velocities along a segment, and ξ_n and ξ_p be the normal and parallel friction coefficients. Now, at every point on a segment, the viscous forces can be resolved into (1) a drag force $(\xi_n/L)v_n$ acting normal to the segment at the point and is due to the normal velocity component, and (2) a drag force $(\xi_p/L)v_p$ acting parallel to the segment at the point and is due to the parallel velocity component.

The total x and y projections of the point normal drag forces can be obtained as shown:

$$\int_0^{L^I} \frac{\xi_n}{L} v_n \cos\theta \, dl = \int_0^{L^{X_I}} \frac{\xi_n}{L} v_n dl^X, \tag{B1a}$$

$$\int_0^{L^I} \frac{\xi_n}{L} v_n \sin\theta \, dl = \int_0^{L^{Y_I}} \frac{\xi_n}{L} v_n dl^Y, \tag{B1b}$$

where l^X and l^Y indicate length projections along the x and y directions, and L^X and L^Y indicate the total length projections in those directions. The notation convention for the different variables is similar to that described in the main text. The superscript indicates the projection of the rod (x or y) to which the variable is affiliated. The subscript to the superscript, when upper case, indicates the segment number with which the variable is associated.

Calculating the projections of the point parallel viscous forces similarly, the net contribution of viscous drag ψ_V^X and ψ_V^Y to the x and y force balance equations [Eqs. (36) and (37)] can be written as

$$\psi_V^{X_I} = \int_0^{L^{X_I}} \frac{\xi_p}{L} v_p dl^X + \int_0^{L^{Y_I}} \frac{\xi_n}{L} v_n dl^Y, \tag{B2}$$

$$\psi_V^{Y_I} = \int_0^{L^{Y_I}} \frac{\xi_p}{L} v_p dl + \int_0^{L^{X_I}} \frac{\xi_n}{L} v_n dl^Y. \tag{B3}$$

Note that the normal viscous forces along the x projection contribute to the force balance in the y direction, and vice versa.

The contribution of the point normal viscous forces to the moment balance, ψ_C in Eq. (35), is

$$\psi_C^I = \int_0^{L^{X_I}} \frac{\xi_n}{L} v_n l^X dl^X + \int_0^{L^{Y_I}} \frac{\xi_n}{L} v_n l^Y dl^Y + \int_0^L \frac{\xi_r}{L^3} \frac{d\theta}{dt} dL. \tag{B4}$$

The moment contribution is calculated similarly to Eq. (21), but using the idea of Eq. (B1). The third term captures the pointwise viscous couple resisting the rotation along the segment. As discussed before, the normal and parallel orientations are assigned based on the configuration of the segment at the *beginning* of a time step. Therefore the point normal and the point parallel viscous forces do not account for the change in orientation along the segment during the time step. The viscous resistance to this orientation change is captured by the third term, where ξ_r is the rotational friction coefficient.

The contribution of the viscous point forces to the change in angle, ψ_θ in Eq. (34), is obtained by integrating the viscous moment contributions over the segment length,

$$\psi_\theta^I = \int_0^{L^{X_I}} \int_0^{L^{X_I}} \frac{\xi_n}{L} v_n l^X dl^X dl^X + \int_0^{L^{Y_I}} \int_0^{L^{Y_I}} \frac{\xi_n}{L} v_n l^Y dl \, dl + \int_0^L \int_0^L \frac{\xi_r}{L^3} \frac{d\theta}{dt} dL \, dL. \tag{B5}$$

The integrations were performed numerically, with about ten integration intervals found sufficient for the simulations in this work.

[1] *Cytoskeletal Mechanics: Models and Measurements*, edited by M. R. K. Mofrad and R. D. Kamm (Cambridge University Press, Cambridge, U.K., 2006).
[2] J. Howard, *Mechanics of Motor Proteins and the Cytoskeleton* (Sinauer Associates, Sunderland, MA, 2001).
[3] O. Kratky and G. Porod, Recl. Trav. Chim. Pays-Bas **68**, 1106 (1949).
[4] J. Wilhelm and E. Frey, Phys. Rev. Lett. **77**, 2581 (1996).
[5] R. F. Feynman, *Feynman Lectures on Physics* (Addison-Wesley Longman, Redwood City, CA, 1970).
[6] D. Thirumalai and B.-Y. Ha, e-print arXiv:cond-mat/9705200.
[7] E. Frey, K. Kroy, and J. Wilhelm, e-print arXiv:cond-mat/9808022v1.
[8] O. Chaudhuri, S. H. Parekh, and D. A. Fletcher, Nature (London) **445**, 295 (2007).
[9] P. A. Janmey, M. E. McCormick, S. Rammensee, J. L. Leight, P. C. Georges, and F. C. MacKintosh, Nature Mater. **6**, 48 (2007).
[10] C. Storm, J. J. Pastore, F. C. MacKintosh, T. C. Lubensky, and P. A. Janmey, Nature (London) **435**, 191 (2005).
[11] D. Ben-Avraham and M. M. Tirion, Biophys. J. **68**, 1231 (1995).
[12] Q. Wen, A. Basu, J. Winer, A. Yodh, and P. A. Janmey, http://adsabs.harvard.edu/abs/2008APS..MAR.R1308W.
[13] Q. Wen, A. Basu, J. P. Winer, A. Yodh, and P. A. Janmey, New J. Phys. **9**, 428 (2007).
[14] D. L. Ermak and J. A. McCammon, J. Chem. Phys. **69**, 1352 (1978).
[15] M. Doi and S. F. Edwards, *The Theory of Polymer Dynamics* (Oxford University Press, New York, 1988).
[16] E. Frey, Ann. Phys. **14**, 20 (2005).
[17] B. Schnurr, F. Gittes, F. C. MacKintosh, and C. F. Schmidt, Macromolecules **30**, 7781 (1997).
[18] A. C. Maggs, Phys. Rev. E **57**, 2091 (1998).
[19] B. Carrasco and J. García de la Torre, J. Chem. Phys. **111**, 4817 (1999).
[20] B. Carrasco and J. G. d. l. Torre, Biophys. J. **76**, 3044 (1999).
[21] P. J. Hagerman and B. H. Zimm, Biopolymers **20**, 1481

(1981).
[22] M. Alberto, D. C. Morse, and P. Matteo, J. Chem. Phys. **122**, 084903 (2005).
[23] M. Lu and J. Ma, Biophys. J. **89**, 2395 (2005).
[24] J. Ma, Curr. Protein Pept. Sci. **5**, 119 (2004).
[25] E. P. Popov, *Engineering Mechanics of Solids* (Prentice-Hall, Englewood Cliffs, NJ, 1999).
[26] A. Ortega and J. G. de la Torre, J. Chem. Phys. **119**, 9914 (2003).
[27] K. E. Bisshopp and D. C. Drucker, Q. Appl. Math. **3**, 272 (1945).
[28] M. A. Ang, Jr., W. Wei, and L. Teck-Sang, in *Industrial Electronics, Control, and Instrumentation, Proceedings of the IECON '93, Maui, HI* (IEEE, Piscataway, NJ, 1993), pp. 1604–1609.
[29] T. Bélendez, M. Pérez-Polo, C. Neip, and A. Beléndez, Phys. Scr., T **118**, 61 (2005).
[30] K. Mattiasson, Int. J. Numer. Methods Eng. **17**, 145 (1980).
[31] F. V. Rohde, Q. Appl. Math. **11**, 337 (1953).
[32] A. Demiroz, Text. Res. J. **75**, 662 (2005).
[33] T. Beléndez, N. Cristian, and A. Beléndez, Eur. J. Phys. **23**, 371 (2002).
[34] L. D. Landau and E. M. Lifshitz, *Theory of Elasticity* (Pergamon Press, New York, 1986).
[35] M. Poirier, S. Eroglu, and J. Marko, Mol. Biol. Cell **13**, 2170 (2002).
[36] F. Gittes, B. Mickey, J. Nettleton, and J. Howard, J. Cell Biol. **120**, 923 (1993).
[37] M. A. Tsai, R. E. Waugh, and P. C. Keng, Biophys. J. **74**, 3282 (1998).
[38] C. P. Brangwynne, G. H. Koenderink, E. Barry, Z. Dogic, F. C. MacKintosh, and D. A. Weitz, Biophys. J. **93**, 346 (2007).
[39] J. Kas, H. Strey, M. Barmann, and E. Sackmann, Europhys. Lett. **21**, 865 (1993).
[40] J. Kas, H. Strey, J. X. Tang, D. Finger, R. Ezzell, E. Sackmann, and P. A. Janmey, Biophys. J. **70**, 609 (1996).
[41] P. L. Chandran and M. R. K. Mofrad (unpublished).